

# Temperature- and Phase-Dependent Phonon Renormalization in 1T'-MoS<sub>2</sub>

Sherman Jun Rong Tan,<sup>†,‡,§</sup> Soumya Sarkar,<sup>‡,§</sup> Xiaoxu Zhao,<sup>†,‡,§</sup> Xin Luo,<sup>‡,||</sup> Yong Zheng Luo,<sup>#,||</sup> Sock Mui Poh,<sup>†,‡</sup> Ibrahim Abdelwahab,<sup>†,‡,§</sup> Wu Zhou,<sup>†,‡,§</sup> Thirumalai Venkatesan,<sup>‡,§,#,○,◆</sup> Wei Chen,<sup>\*,†,#</sup> Su Ying Quek,<sup>\*,‡,#</sup> and Kian Ping Loh<sup>\*,†,‡,§</sup>

<sup>†</sup>Department of Chemistry, National University of Singapore, Singapore 117543

<sup>‡</sup>NUS Graduate School for Integrative Sciences and Engineering, National University of Singapore, Center for Life Sciences, #05-01, 28 Medical Drive, Singapore 117456

<sup>§</sup>NUSNNI-NanoCore, National University of Singapore, 5A Engineering Drive 1, Singapore 117411

<sup>⊥</sup>Center for Advanced 2D Materials and Graphene Research Center, National University of Singapore, Singapore 117546

<sup>||</sup>Department of Applied Physics, The Hong Kong Polytechnic University, Hung Hom, Kowloon, Hong Kong 999077, China

<sup>#</sup>Department of Physics, National University of Singapore, Singapore 117551

<sup>∇</sup>School of Physical Sciences and CAS Center for Excellence in Topological Quantum Computation, University of Chinese Academy of Sciences, Beijing 100049, China

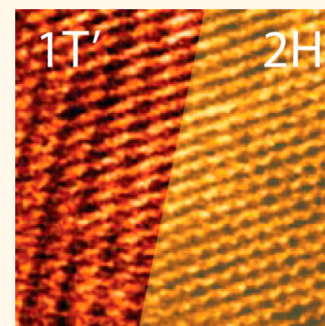
<sup>○</sup>Department of Electrical and Computer Engineering, National University of Singapore, Singapore 117583

<sup>◆</sup>Department of Materials Science and Engineering, National University of Singapore, Singapore 117575

## Supporting Information

**ABSTRACT:** Polymorph engineering of 2H-MoS<sub>2</sub>, which can be achieved by alkali metal intercalation to obtain either the mixed 2H/1T' phases or a homogeneous 1T' phase, has received wide interest recently, since this serves as an effective route to tune the electrical and catalytic properties of MoS<sub>2</sub>. As opposed to an idealized single crystal-to-single crystal phase conversion, the 2H to 1T' phase conversion results in crystal domain size reduction as well as strained lattices, although how these develop with composition is not well understood. Herein, the evolution of the phonon modes in Li-intercalated 1T'-MoS<sub>2</sub> (Li<sub>x</sub>MoS<sub>2</sub>) are investigated as a function of different 1T'-2H compositions. We observed that the strain evolution in the mixed phases is revealed by the softening of four Raman modes, B<sub>g</sub> (J<sub>1</sub>), A<sub>g</sub> (J<sub>3</sub>), E<sup>1</sup><sub>2g</sub>, and A<sub>1g</sub>, with increasing 1T' phase composition. Additionally, the first-order temperature coefficients of the 1T' phonon mode vary linearly with increasing 1T' composition, which is explained by increased electron–phonon and strain–phonon coupling.

**KEYWORDS:** MoS<sub>2</sub>, Raman spectroscopy, vibration, phonon, phase engineering, temperature coefficient



Transition-metal dichalcogenides (TMDs) can manifest in different polymorphs such as 1T, 2H, or 3R with markedly different properties. Due to its thermodynamic instability, the 1T phase readily relaxes to form distorted 1T' phase. The latter has been predicted by theory to exhibit interesting properties such as Weyl semimetallicity<sup>1,2</sup> and quantum spin Hall effect.<sup>3,4</sup> The metallic nature of 1T or 1T'-TMDs has been exploited for hydrogen evolution reaction (HER),<sup>5–7</sup> homojunction contact transistors,<sup>8,9</sup> actuators,<sup>10</sup> and capacitors.<sup>11</sup> A careful survey of published literature reveals two aspects of the 2H-to-1T' phase conversion that are not widely appreciated despite their potential influence on the properties of the material. First, due to the inherent instability of 1T' phase-engineered TMDs, the initially formed 1T' domains can revert to 2H with time, thus these materials actually exist in mixed 2H-1T'

phases, which introduces the possibility of phase domains and associated strains.<sup>12–14</sup> Second, the Mo atom in the parent 1T phase has a three-fold symmetry; thus, dimerization of the Mo sublattice into 1D zigzag chains (*i.e.*, forming the 1T' structure) can happen in three equivalent directions without changing the primary orientation. In other words, the 1T' phase has three orientation variants, resulting from three equivalent directions of structural distortion in the 1T parental phase. Therefore, a 1T' phase conversion will inevitably reduce the crystal domain size due to the statistical tendency to form domain boundaries. Such phase restructuring has been applied previously to improve the

Received: April 10, 2018

Accepted: April 30, 2018

Published: April 30, 2018

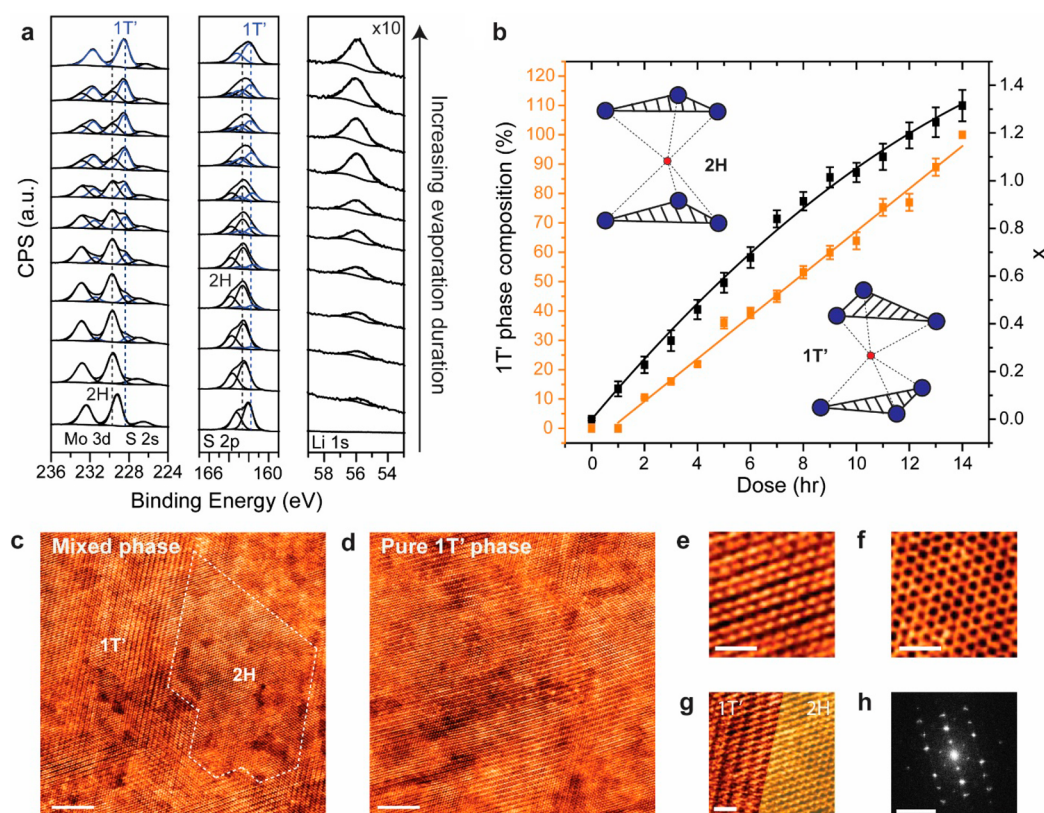


**Figure 1.** (a) XPS spectra showing the evolution of Mo 3d, S 2s, S 2p, and Li 1s core level with increasing lithium evaporation. Peaks assigned to 1T' phase are highlighted in blue. Li core level peaks are magnified 10 times for clarity. (b) Evolution of 1T' phase composition in MoS<sub>2</sub> (left axis) and atomic ratio of Li ( $x$ ) in Li <sub>$x$</sub> MoS<sub>2</sub> (right axis) as a function of lithium dose in hours. (c–d) Annular dark-field scanning transmission electron microscopy (STEM) images of (c) mixed and (d) pure 1T' phase MoS<sub>2</sub>. (e–g) Magnified STEM images of the (e) 1T', (f) 2H, and (g) 1T'/2H interface regions showing the periodic atomic arrangements clearly. (h) FFT pattern of (c). Scale bar is 5 nm in (c–d), 1 nm in (e–g), and 5 nm<sup>-1</sup> in (h).

energy storage performance of MoS<sub>2</sub> batteries.<sup>15</sup> However, there is a lack of systematic study to track the evolution of crystal domains and associated strains in the material during the 2H to 1T' phase conversion. Most published works presume a simple, single crystalline phase conversion without considering how strain as well as occurrence of nanocrystallinity affects ultimate material performance.

Here, we present the phase-dependent and temperature-dependent Raman scattering studies of MoS<sub>2</sub> as a function of 2H/1T' composition. Increasing percentage composition of the 1T' phases in 2H-MoS<sub>2</sub> is achieved by intercalating increasing amounts of Li in 2H-MoS<sub>2</sub>. Raman spectroscopy has been widely used as a powerful nondestructive tool to characterize the different phases in MoS<sub>2</sub>. In addition, the frequency shift of the in-plane E<sub>2g</sub><sup>1</sup> Raman mode can be used to monitor the amount of uniaxial strain in 2H-MoS<sub>2</sub>.<sup>16</sup> However, no systematic studies of 1T'-MoS<sub>2</sub> Raman modes as a function of 2H and 1T' composition have been reported thus far. In this work, we find that the Raman frequencies of B<sub>g</sub> (J<sub>1</sub>), A<sub>g</sub> (J<sub>3</sub>), E<sub>2g</sub><sup>1</sup>, and A<sub>1g</sub> peaks redshift monotonously with the increasing amount of 1T'-MoS<sub>2</sub> in the mixed phase MoS<sub>2</sub>. The phonon softening is interpreted on the basis of strain. We also observed a linear dependence for the temperature coefficients of the 1T' phase Raman modes with increasing 1T' phase/Li intercalation.

## RESULTS AND DISCUSSION

1T'-Li <sub>$x$</sub> MoS<sub>2</sub> is prepared by a first-order Li intercalation of 2H-MoS<sub>2</sub> from a standard SAES getter source (see Methods). The

1T' phase composition can be monitored by X-ray photoemission spectroscopy (XPS) as shown in Figure 1a. A chemical shift of Mo 3d core level peaks by -0.8 eV can be observed, which is due to the reduction of Mo by Li upon 2H to 1T' phase conversion, consistent with earlier studies.<sup>17,18</sup> The phase composition can be obtained by integrating the area under the Mo 3d and S 2p core level peaks fitted with a mixed Gaussian–Lorentzian line-shape with a Shirley background subtraction and is plotted in Figure 1b. At a Li flux of 0.3 ML/h, the 1T' phase formation rate is determined to be 7(±0.3) %/h. A plot of phase composition against Li amount is provided in Figure S1. We find that 100% 1T' phase can be obtained when  $x > 1.3$  in Li <sub>$x$</sub> MoS<sub>2</sub>. The atomic structure of MoS<sub>2</sub> is scrutinized by transmission electron microscopy (TEM) as shown in Figure 1c–h. Figure 1c,d shows the large-scale image of selected mixed phase and pure 1T' phase MoS<sub>2</sub>, respectively. The 1T' phase can be identified by alternating zigzag Mo chains shown in Figure 1e, and the long-range periodic order is indicated by the fast Fourier transform (FFT) spots of 0.17 Å<sup>-1</sup> spacing as shown in Figure 1h. Our TEM results confirm that 2H and 1T' phases coexist with atomically sharp boundaries with no visible defects (Figure 1g).

Raman spectroscopy is sensitive to domain size reduction and lattice strain in 2D materials. Density functional theory (DFT) calculations were performed on 2H and 1T'-MoS<sub>2</sub> based on the rectangular-shaped Brillouin zone (space group P2<sub>1</sub>/m11) as shown in Figure 2a. The irreducible representation for zone center phonons in single layer T' MoS<sub>2</sub> is

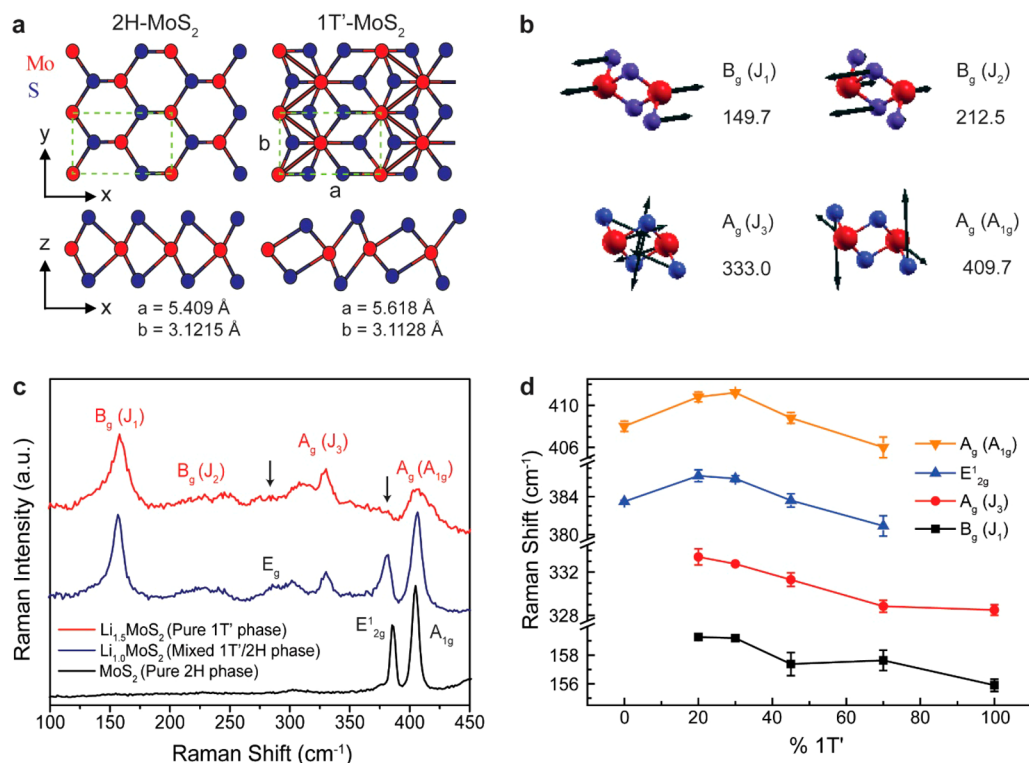


Figure 2. (a) Top (top panel) and side view (bottom panel) atomic structures of 2H and 1T' phase MoS<sub>2</sub> with lattice constants indicated. The dotted rectangle is the surface unit cell. (b) Schematic representations of the motion of atoms for calculated Raman active modes in 1T'-MoS<sub>2</sub>. The symmetry notations follow from group theory, while the notations in brackets do not follow the symmetric point group of the T' phase, but are given for comparison with the literature.<sup>19</sup> The frequencies given below each mode are the computed frequencies (in cm<sup>-1</sup>) for pristine 1T'-MoS<sub>2</sub> with no charge. (c) Raman spectra of Li<sub>x</sub>MoS<sub>2</sub> showing the evolution of Raman modes with increasing lithium content ( $x$ ) with background subtraction. MoS<sub>2</sub> transforms from the 2H phase to pure 1T' phase and the Raman modes originating from the 2H (1T') phase are highlighted in black (red). The arrows indicate peaks absent in the 1T' phase but present in the 2H phase. (d) Phase-dependent Raman shift of B<sub>g</sub>(J<sub>1</sub>), A<sub>g</sub>(J<sub>3</sub>), E<sub>12g</sub>' and A<sub>g</sub>(A<sub>1g</sub>) modes.

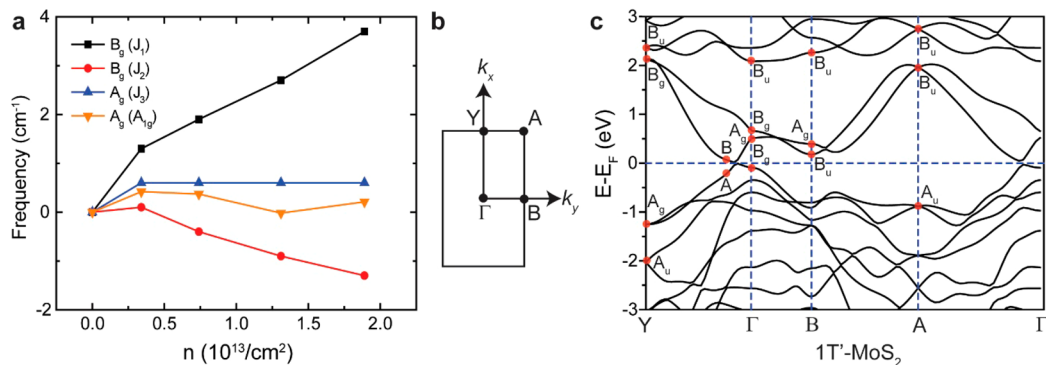
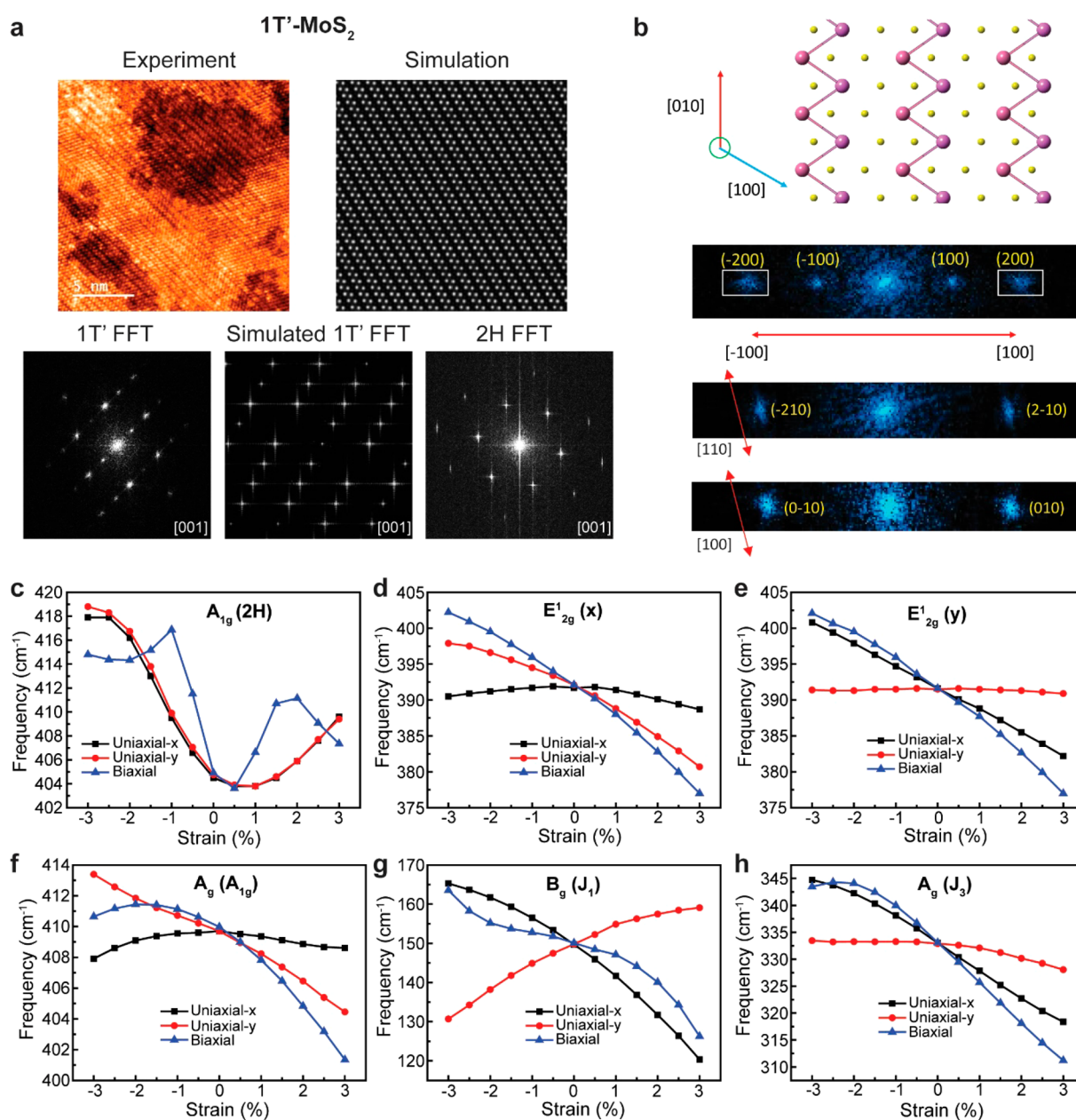


Figure 3. (a) Simulated electron doping effect on the phonon frequencies of 1T'-MoS<sub>2</sub>. (b) Illustration of 2D surface Brillouin zone. The high-symmetry points are marked by black circles. (c) Irreducible representations of 1T'-MoS<sub>2</sub> bands. Red dots indicate the points used for symmetry classification.

$$\Gamma_{\text{layer}} = 6A_g + 3B_g + 6B_u + 3A_u$$

There are nine Raman active modes ( $6A_g + 3B_g$ ) and nine Infrared active modes ( $6B_u + 3A_u$ ). In Figure 2b, we illustrate the atomic motion in the phonon modes that have large enough intensity to be observed in experiment (Figure 2c), together with their computed frequencies for the charge neutral 1T'-MoS<sub>2</sub> monolayer. Notations in brackets follow those in the literature.<sup>19</sup> Atomic motions for the other Raman-active modes can be found in Supplementary Figure S2. Figure 2c shows the representative Raman spectra of 2H and 1T'-Li<sub>x</sub>MoS<sub>2</sub>. 2H-MoS<sub>2</sub> can be

identified by zone center Raman modes at 383 cm<sup>-1</sup> (in-plane E<sub>12g</sub>' mode) and 409 cm<sup>-1</sup> (out-of-plane A<sub>1g</sub> mode). Li<sub>1.0</sub>MoS<sub>2</sub> exhibits 1T' signature Raman modes at 156 (J<sub>1</sub> mode), 228 (J<sub>2</sub> mode), and 330 cm<sup>-1</sup> (J<sub>3</sub> mode) which further confirms the presence of 1T' phase.<sup>20</sup> Additionally, we observed the disorder-allowed E<sub>g</sub> mode originating from 2H-MoS<sub>2</sub> at 285 cm<sup>-1</sup> probably due to intercalation-induced strain. The disappearance of E<sub>g</sub> and E<sub>12g</sub>' modes in Li<sub>1.5</sub>MoS<sub>2</sub> verifies the full conversion to 1T'-MoS<sub>2</sub> as these modes originate from the 2H phase.<sup>21</sup> To disambiguate the peak at 409 cm<sup>-1</sup> since Raman spectroscopy is unable to resolve the contribution from the 1T' or 2H phase, the



**Figure 4.** (a) Experimental and simulated 1T'-MoS<sub>2</sub> TEM and FFT taken along the zone axis [001] direction. FFT of 2H-MoS<sub>2</sub> is shown as a comparison. (b) Comparison of FFT taken along different crystal orientations sharing three-fold symmetry. (c–h) Theoretical strain-mediated Raman frequency shifts in (c–e) 2H-MoS<sub>2</sub> and (f–h) 1T'-MoS<sub>2</sub> for (c) A<sub>1g</sub> (2H), (d) E<sup>1</sup><sub>2g</sub> (x), (e) E<sup>1</sup><sub>2g</sub> (y), (f) A<sub>g</sub> (A<sub>1g</sub>), (g) B<sub>g</sub> (J<sub>1</sub>), and (h) A<sub>g</sub> (J<sub>3</sub>) modes. The double degeneracy of in-plane E<sup>1</sup><sub>2g</sub> mode breaks under the uniaxial strain, that is, (d) E<sup>1</sup><sub>2g</sub> with atoms moving along the armchair direction and (e) E<sup>1</sup><sub>2g</sub> with atoms moving along the zigzag direction.

terminology A<sub>1g</sub> will be used to describe the peak in general, while specific mentions of A<sub>1g</sub> (2H) or A<sub>g</sub> (A<sub>1g</sub>) will be made to denote the 2H or 1T' phase, respectively. Figure 2d shows the phase-dependent Raman shift of B<sub>g</sub> (J<sub>1</sub>), A<sub>g</sub> (J<sub>3</sub>), E<sup>1</sup><sub>2g</sub> and A<sub>1g</sub> modes. Interestingly, both the 2H and 1T' Raman modes soften as the 1T' phase composition increases beyond 30%. Specifically, we observed that the phonon frequencies of 1T' modes B<sub>g</sub> (J<sub>1</sub>) and A<sub>g</sub> (J<sub>3</sub>) decrease by 3.37 and 4.90 cm<sup>-1</sup> when the 1T' phase composition increases from 20% to 100%, respectively. The E<sup>1</sup><sub>2g</sub> and A<sub>1g</sub> Raman modes undergo a stiffening of 2.72 and 3.21 cm<sup>-1</sup> with respect to the pure 2H phase, respectively, which peaks around 20–30% 1T' phase before undergoing phonon softening of 5.28 and 7.41 cm<sup>-1</sup>, respectively. Most strikingly, by taking a linear fit model for the phonon softening of the E<sup>1</sup><sub>2g</sub> and A<sub>1g</sub>

modes, we found that these two modes have the same rate of frequency shift, 0.11 cm<sup>-1</sup>/%, with increase in 1T' composition. This allows the Raman frequencies to serve as an indicator of 1T' phase composition.

The atomic vibration of intercalated van der Waal's materials is known to be modulated by doping, strain, and defects. For example, in the 2H phase, the out-of-plane A<sub>1g</sub> mode for MoS<sub>2</sub> bears the identity representation, which is found to be sensitive to electron doping and long-range Coulombic interactions.<sup>22</sup> In order to interpret the doping effect on electron–phonon coupling in 1T'-MoS<sub>2</sub>, a complete knowledge of the electronic structure and the symmetry information on different bands is required. The electron doping effect on the Raman frequencies for 1T'-MoS<sub>2</sub> based on DFT calculations is presented in Figure

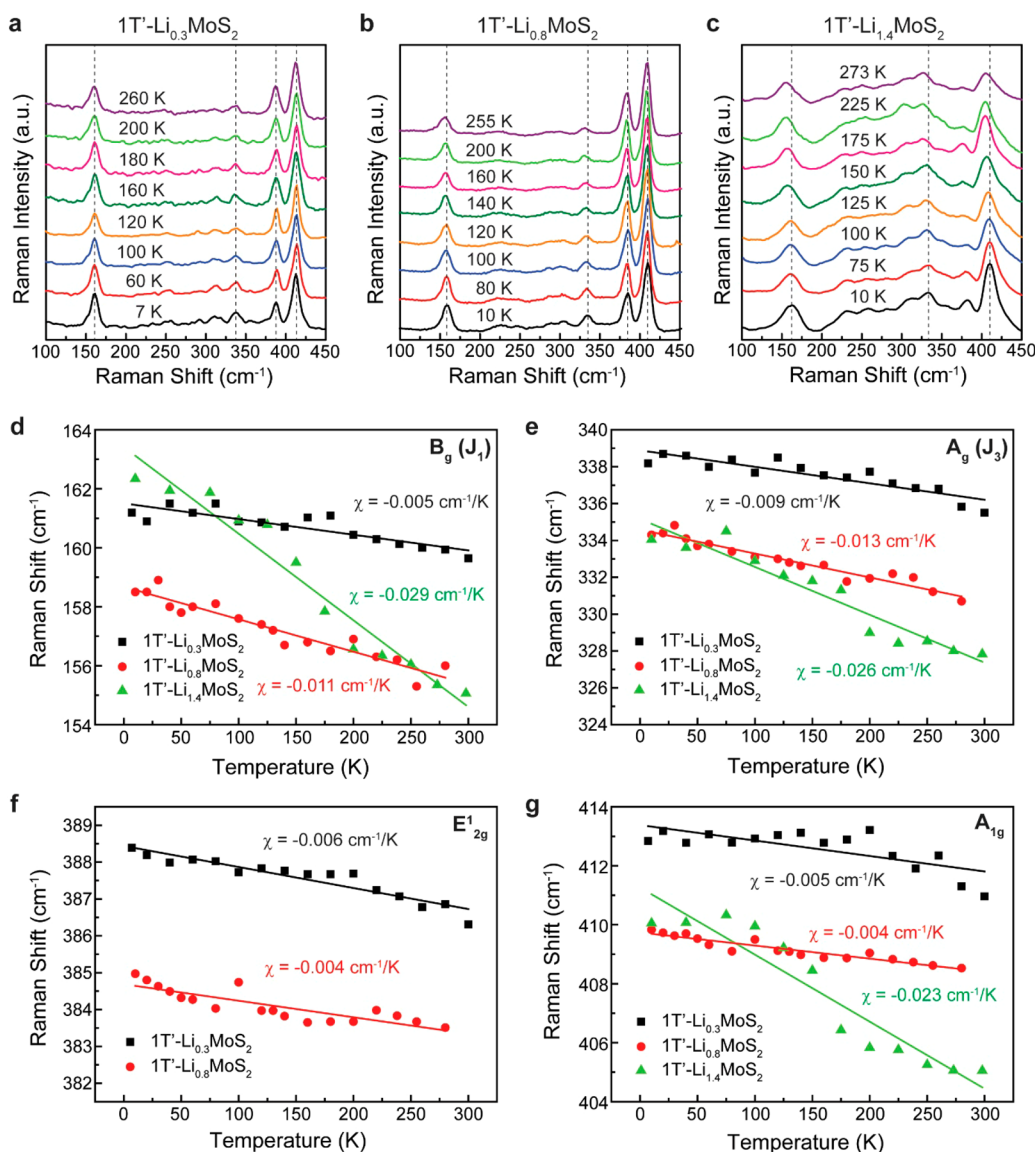


**Figure 5.** (a–c) Raman spectra of  $\text{Li}_{0.3}\text{MoS}_2$  (a),  $\text{Li}_{0.8}\text{MoS}_2$  (b), and  $\text{Li}_{1.4}\text{MoS}_2$  (c) recorded at different temperatures. (d–g) Temperature dependence of the frequencies of Raman active (d)  $B_g(J_1)$ , (e)  $A_g(J_3)$ , (f)  $E_{2g}^1$  and (g)  $A_{1g}$  modes in  $\text{Li}_x\text{MoS}_2$ .

3a. It is shown that the  $A_g(J_3)$  mode has a weak doping dependence. Additionally, our simulation results show that the  $B_g(J_1)$  mode exhibits a blueshift with increasing electron doping, in contrary to our experimentally observed redshift. To further verify our results, we performed group theory analysis of symmetry, as shown in detail in the [Supporting Information](#). The band structures for both 2H and 1T'- $\text{MoS}_2$  are calculated by adopting the same rectangular-shaped Brillouin zone (space group  $P2_1/m11$ ) as shown in [Figure 3b](#). The corresponding irreducible representations of different bands are shown in [Figures S3](#) and [3c](#), respectively. The red dots mark the points used for symmetry classification. With an increase in doping concentration, the highest occupied state (HOS) at the  $\Gamma$  point changes from  $B_g$  to  $A_g$ . When the HOS is  $B_g$ , phonon modes bearing either symmetry will have a nonzero frequency shift (coupling the HOS to the lowest unoccupied states,  $A_g$  and  $B_g$ ). However, when the HOS is  $A_g$ , only the phonon modes with  $B_g$  symmetry have a nonvanishing electron–phonon coupling contribution. This indicates that as doping concentration increases, only the frequencies of the  $B_g$  phonon modes will

change due to electron–phonon coupling. These results are consistent with the frequencies computed by DFT in [Figure 3a](#). As such, electron doping cannot account for the observed phonon shifts in  $\text{Li}_x\text{MoS}_2$  since experimental data and theoretical calculations differ; phonon softening of  $B_g(J_1)$  mode was observed experimentally, but calculations show phonon hardening due to electron doping, and similarly, although  $A_g(J_3)$  and  $A_g(A_{1g})$  modes were simulated to be unaffected by electron doping, it was experimentally observed that  $A_g(J_3)$  mode softens while  $A_g(A_{1g})$  stiffens then softens.

Defects play a profound role in influencing the Raman frequencies of a material as well. It has been found that the separation between the  $E_{2g}^1$  and  $A_{1g}$  modes increases as a function of sulfur vacancy concentration.<sup>23</sup> However, the Mo:S ratio has been found constant throughout the intercalation process ([Figure S4](#)). Additionally, the intercalated Li ions were not considered as defects, but part of the system since Li ions are needed to generate the doping effect required for phase transformation. Therefore, it is unlikely that doping and defects

would play a major role in explaining the phonon redshift behavior observed in our experiments.

In-plane strain has been observed by TEM in alkali metal intercalated  $\text{MoS}_2$ .<sup>24,25</sup> However, no systematic studies have been carried out thus far. In order to understand the observed phonon softening behavior in  $1\text{T}'\text{-MoS}_2$ , strain analysis was performed using TEM and DFT calculations as shown in Figure 4. The experimental and simulated TEM images of pure  $1\text{T}'\text{-MoS}_2$  and their corresponding FFTs taken along the zone axis [001] direction are shown in Figure 4a. Evidently, anisotropic broadening of FFT spots in  $\text{Li}_x\text{MoS}_2$  can be observed. In contrast, FFT of exfoliated  $2\text{H-MoS}_2$  (Figure S5) exhibits perfect round shaped spots. The anisotropic broadening of FFT spots in  $1\text{T}'\text{-MoS}_2$  indicates the presence of strain. Figure 4b shows the experimental FFTs taken along different crystal orientations indicated by a red arrow. The indices of the spots are indicated in yellow. As marked by a white box, it can be observed that the shape of the {200} plane evolves into a rectangular shape along the [100] direction. By further comparing the broadening orientations of the FFT spots sharing a three-fold symmetry, it is observed that the broadening of spots is present in both [100] and [110] directions, which have the  $x$  axis component. Therefore, it can be concluded that there is a predominant strain along the  $x$  axis. DFT simulations were performed to investigate the effects of strain on the Raman spectra of  $\text{Li}_x\text{MoS}_2$ . The strain-mediated Raman frequencies for  $2\text{H-MoS}_2$  and  $1\text{T}'\text{-MoS}_2$  Raman modes corresponding to those analyzed in Figure 2d are plotted in Figure 4c–e and 4f–h, respectively. Strain-mediated Raman frequency for  $\text{B}_g$  ( $J_2$ ) can be found in Supporting Information (Figure S6). The shift in the frequencies of the Raman modes as a function of  $1\text{T}'$  content in the current study is consistent with the increase in tensile strain of  $\text{Li}_x\text{MoS}_2$  and can be explained by a combination of biaxial and uniaxial tensile strains along the  $x$  axis. It should be noted that TEM is unable to conclude the presence of biaxial strain since isotropic broadening of FFT spots can have other origins. Under a combination of biaxial and uniaxial tensile strain along the  $x$  axis, the  $\text{A}_{1g}$ ,  $\text{E}_{2g}^1$ ,  $\text{B}_g$  ( $J_1$ ), and  $\text{A}_g$  ( $J_3$ ) modes soften with increasing strain, consistent with experimental data.

The formation of Mo zigzag clusters has been attributed to charge density wave (CDW) phenomenon by earlier studies.<sup>26,27</sup> It would therefore be of interest to investigate the electron–phonon interactions of  $\text{Li}_x\text{MoS}_2$  through a temperature-dependent Raman study. Figure 5 shows the temperature evolution of zone-center phonon  $\text{B}_g$  ( $J_1$ ),  $\text{A}_g$  ( $J_3$ ),  $\text{E}_{2g}^1$  and  $\text{A}_{1g}$  modes of  $\text{Li}_x\text{MoS}_2$  at different lithium concentrations. As temperature increases, all peaks shift toward lower frequencies, and the redshift is more pronounced for  $1\text{T}'$  than  $2\text{H}$  Raman modes. This temperature-dependent shift can be attributed to electron–phonon interactions, thermal expansion, or anharmonic contributions to the interatomic potential energy, which are mediated by phonon–phonon interactions.<sup>28</sup>

Generally, the softening of Raman modes as temperature increases is consistent with the reduction of interlayer coupling.<sup>29</sup> The temperature-dependent peaks were fitted using the Grüneisen model equation:<sup>30</sup>

$$\omega(T) = \omega_0 + \chi T \quad (1)$$

where  $\omega_0$  is the frequency of vibration at absolute zero temperature and  $\chi$  is the first-order temperature coefficient of the mode. The slope of the fitted straight line represents the value of  $\chi$ , and the detailed plots can be found in Figure 5. We obtained  $\chi$  values of  $-0.0294$ ,  $-0.0260$ , and  $-0.0227$   $\text{cm}^{-1}/\text{K}$  for the  $\text{B}_g$

( $J_1$ ),  $\text{A}_g$  ( $J_3$ ), and  $\text{A}_g$  ( $\text{A}_{1g}$ ) modes of  $1\text{T}'\text{-Li}_{1.4}\text{MoS}_2$ , respectively. The obtained  $\chi$  values for  $1\text{T}'\text{-Li}_x\text{MoS}_2$  are larger than reported  $2\text{H-MoS}_2$  ( $\chi = -0.013$  and  $-0.015$   $\text{cm}^{-1}/\text{K}$  for  $\text{A}_{1g}$  and  $\text{E}_{2g}$  modes,<sup>31</sup> respectively) and other 2D materials such as graphene ( $\chi = -0.016$   $\text{cm}^{-1}/\text{K}$  for G mode)<sup>32</sup> and  $\text{MoSe}_2$  ( $\chi = -0.0054$  and  $-0.0086$   $\text{cm}^{-1}/\text{K}$  for  $\text{A}_{1g}$  and  $\text{A}_{2u}^2$  modes,<sup>30</sup> respectively). This is consistent with the possibility of an increased strain–phonon coupling (shift in phonon frequencies under the effects of strain) in  $\text{Li}_x\text{MoS}_2$  since our DFT results indicate that the electron–phonon coupling is stronger for  $\text{B}_g$  ( $J_1$ ) mode compared to  $\text{A}_g$  ( $J_3$ ) mode, yet the temperature coefficients for both Raman modes are of similar magnitude.<sup>30</sup> Furthermore, with increasing  $1\text{T}'$  content, the  $1\text{T}'$  Raman peaks evolve from a Lorentzian shape to a Breit–Wigner (BW) shape as exemplified in Figure 5c.

The BW line shape can be described by the following equation:<sup>33</sup>

$$I(\omega) = \frac{I_0 \left[ 1 + \frac{2(\omega - \omega_0)}{Q\Gamma} \right]^2}{1 + \left[ \frac{2(\omega - \omega_0)}{\Gamma} \right]^2} \quad (2)$$

where  $\omega_0$  is the peak position,  $I_0$  is the peak intensity,  $\Gamma$  is the fwhm, and  $Q$  is the BW coefficient. As  $Q^{-1} \rightarrow 0$ , the Lorentzian line shape is recovered. The BW resonance arises due to phonon coupling with an electron continuum, commonly observed in stage-I graphite intercalated compounds.<sup>34</sup> This would further explain the larger temperature coefficient of  $\text{Li}_x\text{MoS}_2$  when pure  $1\text{T}'$  phase is attained. Our results suggest that the  $2\text{H}$  to  $1\text{T}'$  phase transition in  $\text{MoS}_2$  is accompanied by an increased electron–phonon coupling. However, since electron doping is unable to account for the phonon softening behavior upon phase transformation, it would imply that strain plays a dominant role in the Raman spectra of  $2\text{H-}1\text{T}'$   $\text{Li}_x\text{MoS}_2$ , possibly by mediating the phase transition by lowering the energy barrier.<sup>35</sup>

The phase-dependent  $\chi$  values are plotted in Figure 6. The magnitude of the temperature coefficient for  $2\text{H}$  modes

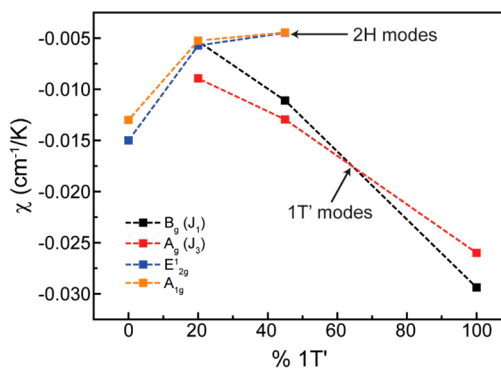


Figure 6. Phase-dependent first-order temperature coefficient of  $\text{Li}_x\text{MoS}_2$ .

decreases rapidly with increasing  $1\text{T}'$  content (and Li amount), while that of the  $1\text{T}'$  modes increases almost linearly. This provides another handle for the determination of the  $1\text{T}'$  phase content in  $\text{Li}_x\text{MoS}_2$ . Furthermore, since the temperature coefficients of  $2\text{H}$  and  $1\text{T}'\text{-Li}_x\text{MoS}_2$  are vastly different in magnitude, it can be used to distinguish the two phases.

## CONCLUSIONS

In conclusion, a systematic study of the phase and temperature dependence of the phonon modes in 1T'-Li<sub>x</sub>MoS<sub>2</sub> phase was performed. We observed that 2H and 1T' Raman modes redshift with increasing 1T' phase content, which can be predominantly attributed to strain. The evolution of a Breit–Wigner resonance line shape with increasing 1T' phase indicates increased electron–phonon coupling, which is further confirmed by a larger temperature coefficient of the lithium-intercalated 1T' phase modes compared to the 2H modes. The similar temperature coefficients of the B<sub>g</sub> (J<sub>1</sub>) and A<sub>g</sub> (J<sub>3</sub>) Raman modes despite their different electron–phonon coupling strength as revealed by our DFT calculations can be explained by an increased in strain–phonon coupling, which is consistent with our phase-dependent Raman results. Our results highlight the importance of strain–phonon coupling in 1T'-Li<sub>x</sub>MoS<sub>2</sub>. Taken together, these spectroscopic signatures can be used as a tool to monitor the relative content of the 2H-1T' phases in alkali metal intercalated transition-metal dichalcogenides.

## METHODS

**Sample Preparation.** The MoS<sub>2</sub> crystals used are synthetic single crystals purchased from HQGraphene. Few-layered MoS<sub>2</sub> (3–5 nm) on SiO<sub>2</sub> samples are obtained using scotch tape exfoliation from synthetic single crystals. The samples were annealed in an ultrahigh-vacuum chamber system of base pressure  $4 \times 10^{-10}$  Torr at 573 K for 1 h. Alkali metal was introduced from a commercial SAES getter source at a rate of  $\sim 0.3$  ML/h. The source was thoroughly degassed before each deposition to minimize contamination. Intercalation and passivation methods are described in previous reports.<sup>36</sup>

**Sample Characterization.** XPS characterizations were carried out using SPECS XR-50 X-ray Mg K $\alpha$  (1253.7 eV) source with the pass energy of 30 eV and spot size of 5 mm. Detection is done by a PHOIBOS 150 hemispherical energy analyzer (SPECS, GmbH) equipped with a 3D delay line detector (3D-DLD, SPECS GmbH). The binding energies of the XPS spectra were calibrated to the Au 4f<sub>7/2</sub> peaks. XPS peak fitting was carried out using a mixed Gaussian–Lorentzian function after a Shirley background subtraction. An area ratio of 3:2 between the Mo 3d<sub>5/2</sub> and 3d<sub>3/2</sub> peaks and an area ratio of 2:1 between the S 2p<sub>3/2</sub> and 2p<sub>1/2</sub> peaks were employed in the fit with same fwhm. The spin–orbit splitting for Mo 3d and S 2p spectra are 3.15 and 1.18 eV respectively.

Room-temperature Raman spectroscopy was performed using a WiTec Alpha 300R confocal Raman microscope with an excitation wavelength of 532 nm and a laser power of  $< 500 \mu\text{W}$ . The laser was focused on the samples using 100 $\times$  air-objective, and a spectral grating with 1800 lines/mm was used for all Raman spectra.

Low-temperature Raman spectroscopy measurements were done using a JY Horiba LabRAM HR Evolution Raman Spectrometer coupled with an air-cooled CCD. All the data have been recorded at an excitation wavelength of 514.5 nm from a Lexel SHG 95 argon ion laser. The laser power incident on the sample is estimated to be  $< 400 \mu\text{W}$ . The spectra were collected at periodic temperature intervals from 10 to 300 K to understand the temperature dependence using an Advanced Research Systems Inc. compressed helium-based closed cycle refrigerator coupled with the above spectrometer.

STEM ADF imaging was carried on an aberration-corrected Nion UltraSTEM-100, equipped with a cold field emission gun, operating at 60 kV. The convergence semiangle for the incident probe was set to 31 mrad, with a half angle range from  $\sim 86$  to 200 mrad. The dwell time for single-scan imaging is set to be 18  $\mu\text{s}$ /pixel. All imaging was performed at room temperature. In order to eliminate possibility of anisotropic spot broadening caused by sample tilt, analysis was performed on numerous FFTs taken from random locations. Additionally, all MoS<sub>2</sub> samples were carefully tilted to the [001] zone axis before characterization.

**Calculation Details.** First-principles calculations of the vibrational modes are performed within density functional theory (DFT) as implemented in the projector augmented wave pseudopotential code

Vienna *ab Initio* Simulation Package.<sup>37</sup> 14 electrons are considered explicitly as valence electrons in the Mo pseudopotential. In the DFT calculations, the exchange–correlation effects are described by the local density approximation (LDA).<sup>38</sup> To get converged results, wave functions are expanded in a plane-wave basis set with a kinetic energy cutoff of 400 eV. The phonon frequencies and eigenmodes of the T' phase were found to be unchanged for an increased energy cutoff of 500 eV. The convergence thresholds are set to  $1 \times 10^{-8}$  eV and 0.001 eV/Å for the electronic self-consistent loop and ionic relaxation loop, respectively. A vacuum thickness of more than 16 Å is added in the unit cell to prevent interactions between slabs. All atomic positions, and the cell size and shape, were relaxed. To apply the uniaxial strains along the zigzag and armchair directions of the 2H phase MoS<sub>2</sub>, the rectangle representation is used in the calculation. A Monkhorst–Pack *k*-point mesh of  $8 \times 15 \times 1$  is used to sample the Brillouin Zones for the thin films systems. In order to simulate the electron doping effect in the system, we add extra electrons into the unit cell with a neutralizing background charge. The phonon frequencies are calculated with the fully relaxed structures using the density functional perturbation theory method.

## ASSOCIATED CONTENT

### Supporting Information

The Supporting Information is available free of charge on the ACS Publications website at DOI: 10.1021/acsnano.8b02649.

Experimental details and supporting figures (PDF)

## AUTHOR INFORMATION

### Corresponding Authors

\*E-mail: chmlhkp@nus.edu.sg.

\*E-mail: phyqsy@nus.edu.sg.

\*E-mail: phycw@nus.edu.sg.

### ORCID

Sherman Jun Rong Tan: 0000-0003-1591-3497

Xiaoxu Zhao: 0000-0001-9746-3770

Yong Zheng Luo: 0000-0002-5142-2508

Ibrahim Abdelwahab: 0000-0002-0107-5827

Wu Zhou: 0000-0002-6803-1095

Kian Ping Loh: 0000-0002-1491-743X

### Notes

The authors declare no competing financial interest.

## ACKNOWLEDGMENTS

K.P.L. and S.Y.Q. are grateful to the funding from the National Research Foundation, Prime Minister's Office, Mid-sized Research Centre (CA2DM). S.Y.Q. acknowledges grant no. NRF-NRFF2013-07. X.L. acknowledges the Hong Kong Polytechnic University grant (no.: G-UABC). T.V. would like to acknowledge support from the National Research Foundation under Competitive Research Program (NRF2015NRF-CRP001-015). This research was also supported in part by the U.S. Department of Energy, Office of Science, Basic Energy Science, Materials Sciences and Engineering Division (W.Z.), and through a user project at ORNL's Center for Nanophase Materials Sciences (CNMS), which is a DOE Office of Science User Facility. Computations were performed on the computational cluster of CA2DM.

## REFERENCES

- (1) Deng, K.; Wan, G.; Deng, P.; Zhang, K.; Ding, S.; Wang, E.; Yan, M.; Huang, H.; Zhang, H.; Xu, Z.; Denlinger, J.; Fedorov, A.; Yang, H.; Duan, W.; Yao, H.; Wu, Y.; Fan, S.; Zhang, H.; Chen, X.; Zhou, S.

Experimental Observation of Topological Fermi Arcs in Type-II Weyl Semimetal MoTe<sub>2</sub>. *Nat. Phys.* **2016**, *12*, 1105–1110.

(2) Huang, L.; McCormick, T. M.; Ochi, M.; Zhao, Z.; Suzuki, M. T.; Arita, R.; Wu, Y.; Mou, D.; Cao, H.; Yan, J.; Trivedi, N.; Kaminski, A. Spectroscopic Evidence for a Type II Weyl Semimetallic State in MoTe<sub>2</sub>. *Nat. Mater.* **2016**, *15*, 1155–1160.

(3) Qian, X.; Liu, J.; Fu, L.; Li, J. Quantum Spin Hall Effect in Two-Dimensional Transition Metal Dichalcogenides. *Science* **2014**, *346*, 1344–1347.

(4) Tang, S.; Zhang, C.; Wong, D.; Pedramrazi, Z.; Tsai, H.-Z.; Jia, C.; Moritz, B.; Claassen, M.; Ryu, H.; Kahn, S.; Jiang, J.; Yan, H.; Hashimoto, M.; Lu, D.; Moore, R. G.; Hwang, C.-C.; Hwang, C.; Hussain, Z.; Chen, Y.; Ugeda, M. M.; et al. Quantum Spin Hall State in Monolayer 1T'-WTe<sub>2</sub>. *Nat. Phys.* **2017**, *13*, 683–687.

(5) Voiry, D.; Salehi, M.; Silva, R.; Fujita, T.; Chen, M.; Asefa, T.; Shenoy, V. B.; Eda, G.; Chhowalla, M. Conducting MoS<sub>2</sub> Nanosheets as Catalysts for Hydrogen Evolution Reaction. *Nano Lett.* **2013**, *13*, 6222–6227.

(6) Chang, K.; Hai, X.; Pang, H.; Zhang, H.; Shi, L.; Liu, G.; Liu, H.; Zhao, G.; Li, M.; Ye, J. Targeted Synthesis of 2H- and 1T-Phase MoS<sub>2</sub> Monolayers for Catalytic Hydrogen Evolution. *Adv. Mater.* **2016**, *28*, 10033–10041.

(7) Chen, Z.; Leng, K.; Zhao, X.; Malkhandi, S.; Tang, W.; Tian, B.; Dong, L.; Zheng, L.; Lin, M.; Yeo, B. S.; Loh, K. P. Interface Confined Hydrogen Evolution Reaction in Zero Valent Metal Nanoparticles-Intercalated Molybdenum Disulfide. *Nat. Commun.* **2017**, *8*, 14548.

(8) Kappera, R.; Voiry, D.; Yalcin, S. E.; Branch, B.; Gupta, G.; Mohite, A. D.; Chhowalla, M. Phase-Engineered Low-Resistance Contacts for Ultrathin MoS<sub>2</sub> Transistors. *Nat. Mater.* **2014**, *13*, 1128–1134.

(9) Cho, S.; Kim, S.; Kim, J. H.; Zhao, J.; Seok, J.; Keum, D. H.; Baik, J.; Choe, D.-H.; Chang, K. J.; Suenaga, K.; Kim, S. W.; Lee, Y. H.; Yang, H. Phase Patterning for Ohmic Homojunction Contact in MoTe<sub>2</sub>. *Science* **2015**, *349*, 625–628.

(10) Acerce, M.; Akdogan, E. K.; Chhowalla, M. Metallic Molybdenum Disulfide Nanosheet-based Electrochemical Actuators. *Nature* **2017**, *549*, 370–373.

(11) Acerce, M.; Voiry, D.; Chhowalla, M. Metallic 1T phase MoS<sub>2</sub> Nanosheets as Supercapacitor Electrode Materials. *Nat. Nanotechnol.* **2015**, *10*, 313–318.

(12) Liu, Q.; Fang, Q.; Chu, W.; Wan, Y.; Li, X.; Xu, W.; Habib, M.; Tao, S.; Zhou, Y.; Liu, D.; Xiang, T.; Khalil, A.; Wu, X.; Chhowalla, M.; Ajayan, P. M.; Song, L. Electron-Doped 1T-MoS<sub>2</sub> via Interface Engineering for Enhanced Electrocatalytic Hydrogen Evolution. *Chem. Mater.* **2017**, *29*, 4738–4744.

(13) Kim, J. S.; Kim, J.; Zhao, J.; Kim, S.; Lee, J. H.; Jin, Y.; Choi, H.; Moon, B. H.; Bae, J. J.; Lee, Y. H.; Lim, S. C. Electrical Transport Properties of Polymorphic MoS<sub>2</sub>. *ACS Nano* **2016**, *10*, 7500–7506.

(14) Voiry, D.; Yamaguchi, H.; Li, J.; Silva, R.; Alves, D. C.; Fujita, T.; Chen, M.; Asefa, T.; Shenoy, V. B.; Eda, G.; Chhowalla, M. Enhanced Catalytic Activity in Strained Chemically Exfoliated WS<sub>2</sub> Nanosheets for Hydrogen Evolution. *Nat. Mater.* **2013**, *12*, 850–855.

(15) Leng, K.; Chen, Z.; Zhao, X.; Tang, W.; Tian, B.; Nai, C. T.; Zhou, W.; Loh, K. P. Phase Restructuring in Transition Metal Dichalcogenides for Highly Stable Energy Storage. *ACS Nano* **2016**, *10*, 9208–9215.

(16) Wang, Y.; Cong, C.; Qiu, C.; Yu, T. Raman Spectroscopy Study of Lattice Vibration and Crystallographic Orientation of Monolayer MoS<sub>2</sub> under Uniaxial Strain. *Small* **2013**, *9*, 2857–2861.

(17) Yin, Y.; Miao, P.; Zhang, Y.; Han, J.; Zhang, X.; Gong, Y.; Gu, L.; Xu, C.; Yao, T.; Xu, P.; Wang, Y.; Song, B.; Jin, S. Significantly Increased Raman Enhancement on MoX<sub>2</sub> (X = S, Se) Monolayers upon Phase Transition. *Adv. Funct. Mater.* **2017**, *27*, 1606694.

(18) Eda, G.; Yamaguchi, H.; Voiry, D.; Fujita, T.; Chen, M.; Chhowalla, M. Photoluminescence from Chemically Exfoliated MoS<sub>2</sub>. *Nano Lett.* **2011**, *11*, 5111–5116.

(19) Nayak, A. P.; Pandey, T.; Voiry, D.; Liu, J.; Moran, S. T.; Sharma, A.; Tan, C.; Chen, C. H.; Li, L. J.; Chhowalla, M.; Lin, J. F.; Singh, A. K.; Akinwande, D. Pressure-Dependent Optical and Vibrational Properties of Monolayer Molybdenum Disulfide. *Nano Lett.* **2015**, *15*, 346–353.

(20) Hu, T.; Li, R.; Dong, J. A New (2 × 1) Dimerized Structure of Monolayer 1T-Molybdenum Disulfide, Studied from First Principles Calculations. *J. Chem. Phys.* **2013**, *139*, 174702.

(21) Lee, J. U.; Park, J.; Son, Y. W.; Cheong, H. Anomalous Excitonic Resonance Raman Effects in Few-Layered MoS<sub>2</sub>. *Nanoscale* **2015**, *7*, 3229–3236.

(22) Chakraborty, B.; Bera, A.; Muthu, D. V. S.; Bhowmick, S.; Waghmare, U. V.; Sood, A. K. Symmetry-Dependent Phonon Renormalization in Monolayer MoS<sub>2</sub> Transistor. *Phys. Rev. B: Condens. Matter Mater. Phys.* **2012**, *85*, 161403.

(23) Parkin, W. M.; Balan, A.; Liang, L.; Das, P. M.; Lamparski, M.; Naylor, C. H.; Rodriguez-Manzo, J. A.; Johnson, A. T.; Meunier, V.; Drndic, M. Raman Shifts in Electron-Irradiated Monolayer MoS<sub>2</sub>. *ACS Nano* **2016**, *10*, 4134–4142.

(24) Wang, L.; Xu, Z.; Wang, W.; Bai, X. Atomic Mechanism of Dynamic Electrochemical Lithiation Processes of MoS<sub>2</sub> Nanosheets. *J. Am. Chem. Soc.* **2014**, *136*, 6693–6697.

(25) Wang, X.; Shen, X.; Wang, Z.; Yu, R.; Chen, L. Atomic-Scale Clarification of Structural Transition of MoS<sub>2</sub> upon Sodium Intercalation. *ACS Nano* **2014**, *8*, 11394–11400.

(26) Chen, X.; Chen, Z.; Li, J. Critical Electronic Structures Controlling Phase Transitions Induced by Lithium Ion Intercalation in Molybdenum Disulfide. *Chin. Sci. Bull.* **2013**, *58*, 1632–1641.

(27) Rocquefelte, X.; Boucher, F.; Gressier, P.; Ouvrard, G.; Blaha, P.; Schwarz, K. Mo Cluster Formation in the Intercalation Compound LiMoS<sub>2</sub>. *Phys. Rev. B: Condens. Matter Mater. Phys.* **2000**, *62*, 2397–2400.

(28) Łapińska, A.; Taube, A.; Judek, J.; Zdrojek, M. Temperature Evolution of Phonon Properties in Few-Layer Black Phosphorus. *J. Phys. Chem. C* **2016**, *120*, 5265–5270.

(29) Tongay, S.; Zhou, J.; Ataca, C.; Lo, K.; Matthews, T. S.; Li, J.; Grossman, J. C.; Wu, J. Thermally Driven Crossover from Indirect Toward Direct Bandgap in 2D Semiconductors: MoSe<sub>2</sub> Versus MoS<sub>2</sub>. *Nano Lett.* **2012**, *12*, 5576–5580.

(30) Late, D. J.; Shirodkar, S. N.; Waghmare, U. V.; Dravid, V. P.; Rao, C. N. Thermal Expansion, Anharmonicity and Temperature-Dependent Raman Spectra of Single- and Few-Layer MoSe<sub>2</sub> and WSe<sub>2</sub>. *ChemPhysChem* **2014**, *15*, 1592–1598.

(31) Lanzillo, N. A.; Glen Birdwell, A.; Amani, M.; Crowne, F. J.; Shah, P. B.; Najmaei, S.; Liu, Z.; Ajayan, P. M.; Lou, J.; Dubey, M.; Nayak, S. K.; O'Regan, T. P. Temperature-Dependent Phonon Shifts in Monolayer MoS<sub>2</sub>. *Appl. Phys. Lett.* **2013**, *103*, 093102.

(32) Late, D. J.; Maitra, U.; Panchakarla, L. S.; Waghmare, U. V.; Rao, C. N. R. Temperature Effects on the Raman Spectra of Graphenes: Dependence on the Number of Layers and Doping. *J. Phys.: Condens. Matter* **2011**, *23*, 055303.

(33) Ferrari, A. C.; Robertson, J. Interpretation of Raman Spectra of Disordered and Amorphous Carbon. *Phys. Rev. B: Condens. Matter Mater. Phys.* **2000**, *61*, 14095–14107.

(34) Eklund, P. C.; Subbaswamy, K. R. Analysis of Breit-Wigner Line Shapes in the Raman Spectra of Graphite Intercalation Compounds. *Phys. Rev. B: Condens. Matter Mater. Phys.* **1979**, *20*, 5157–5161.

(35) Ouyang, B.; Xiong, S.; Yang, Z.; Jing, Y.; Wang, Y. MoS<sub>2</sub> Heterostructure with Tunable Phase Stability: Strain Induced Interlayer Covalent Bond Formation. *Nanoscale* **2017**, *9*, 8126–8132.

(36) Tan, S. J.; Abdelwahab, I.; Ding, Z.; Zhao, X.; Yang, T.; Loke, G. Z.; Lin, H.; Verzhbitskiy, I.; Poh, S. M.; Xu, H.; Nai, C. T.; Zhou, W.; Eda, G.; Jia, B.; Loh, K. P. Chemical Stabilization of 1T' Phase Transition Metal Dichalcogenides with Giant Optical Kerr Nonlinearity. *J. Am. Chem. Soc.* **2017**, *139*, 2504–2511.

(37) Kresse, G.; Furthmüller, J. Efficiency of *Ab-Initio* Total Energy Calculations for Metals and Semiconductors Using a Plane-Wave Basis Set. *Comput. Mater. Sci.* **1996**, *6*, 15–50.

(38) Perdew, J. P.; Zunger, A. Self-interaction Correction to Density-Functional Approximations for Many-Electron Systems. *Phys. Rev. B: Condens. Matter Mater. Phys.* **1981**, *23*, 5048–5079.